Mechanism of single- and double-sided inhibition of dual topology fluoride channels by synthetic monobodies

Daniel L. Turman[1] and Randy B. Stockbridge[2,3]

[1]Department of Biochemistry and Howard Hughes Medical Institute, Brandeis University, Waltham, MA 02454
[2]Program in Biophysics and [3]Department of Molecular, Cellular, and Developmental Biology, University of Michigan, Ann Arbor, MI 48109

The Fluc family of proteins comprises small, electrodiffusive fluoride channels, which prevent accumulation of toxic F^- ions in microorganisms. Recent crystal structures have confirmed their unusual architecture, in which a pair of antiparallel subunits convenes to form a dimer with a twofold symmetry axis parallel to the plane of the membrane. These structures have also revealed the interactions between Fluc channels and several different fibronectin domain monobodies that inhibit Fluc-mediated F^- currents; in all structures, each channel binds to two monobodies symmetrically, one on either side of the membrane. However, these structures do not reveal the mechanism of monobody inhibition. Moreover, the results appear to diverge from a recent electrophysiological study indicating that monobody binding is negatively cooperative; that is, a bound monobody on one side of a Fluc channel decreases the affinity of an oppositely bound monobody by ∼10-fold. In this study, we reconcile these observations by probing the mechanism of monobody binding and its negative cooperativity using electrophysiological experiments in planar lipid bilayers. Our results indicate that monobody inhibition occurs via a pore-blocking mechanism and that negative cooperativity arises from electrostatic repulsion between the oppositely bound monobodies. A single glutamate residue, on a loop of the monobody that extends into the channel interior, is responsible for negatively cooperative binding. This glutamate side chain also confers voltage dependence and sensitivity to the concentration of trans-F^- ion to monobody binding. Neutralization by mutation to glutamine abolishes these electrostatic effects. Monobodies that are amenable to cocrystallization with Fluc channels lack an analogous negatively charged side chain and bind independently to opposite sides of the channel. Thus, this work reveals the source of voltage dependence and negative cooperativity of monobody binding to Fluc channels along with the pore-blocking mechanism.

The Journal of General Physiology

INTRODUCTION

The Fluc family of fluoride channels counteracts F^- toxicity in microorganisms by undermining weak acid accumulation of environmental F^- ion (Baker et al., 2012; Stockbridge et al., 2013; Ji et al., 2014). Recent crystal structures of two different Fluc homologues reveal an antiparallel homodimer with twofold symmetry about the plane of the membrane and two antiparallel pores, each with two resolved F^- ions (Stockbridge et al., 2015). The channel is capped by monobody crystallization chaperones, one on each side of the membrane, which wedge loops into a deep cleft between the subunits of the dimer. These monobodies, small synthetic proteins based on a human fibronectin III domain scaffold, were selected from combinatorial libraries and exhibit tight, specific binding to Fluc channels (Koide et al., 2012). Electrophysiological experiments show that several of the monobodies selected to bind Fluc proteins also inhibit F^- current when applied to conducting channels in planar lipid bilayers (Stockbridge et al., 2014, 2015). Because they play dual roles as inhibitors and crystallization chaperones, understanding the mechanism by which they inhibit provides critical context for interpreting crystal structures of Fluc channels. In this paper, we discuss two closely related monobodies: L3, which has been extensively characterized using electrophysiology, and L2, which was used to crystallize the Fluc homologue from *Bordetella pertussis*, Bpe (Stockbridge et al., 2015). The L2 and L3 sequences differ only in an eight-residue loop (Fig. 1).

When applied to either side of the bilayer, monobody L3 blocks Bpe with identical kinetics regardless of the side to which is it is added (Stockbridge et al., 2014). These results appeared to be in harmony with the doubly L2-bound channel observed in the crystal structure. However, recent single-channel experiments show that when L3 is applied to both sides of the channel simultaneously, binding of the second L3 molecule is ∼10-fold weaker than binding of the first, a difference in affinity of ∼1.4 kcal/mol (Turman et al., 2015). The origin of this negative cooperativity is unknown, but two possible mechanisms were suggested: (1) a conformational

Correspondence to Randy B. Stockbridge: stockbr@umich.edu
Abbreviation used: APBS, adaptive Poisson-Boltzmann solver.

The Rockefeller University Press $30.00
J. Gen. Physiol. 2017 Vol. 149 No. 4 511–522
https://doi.org/10.1085/jgp.201611747

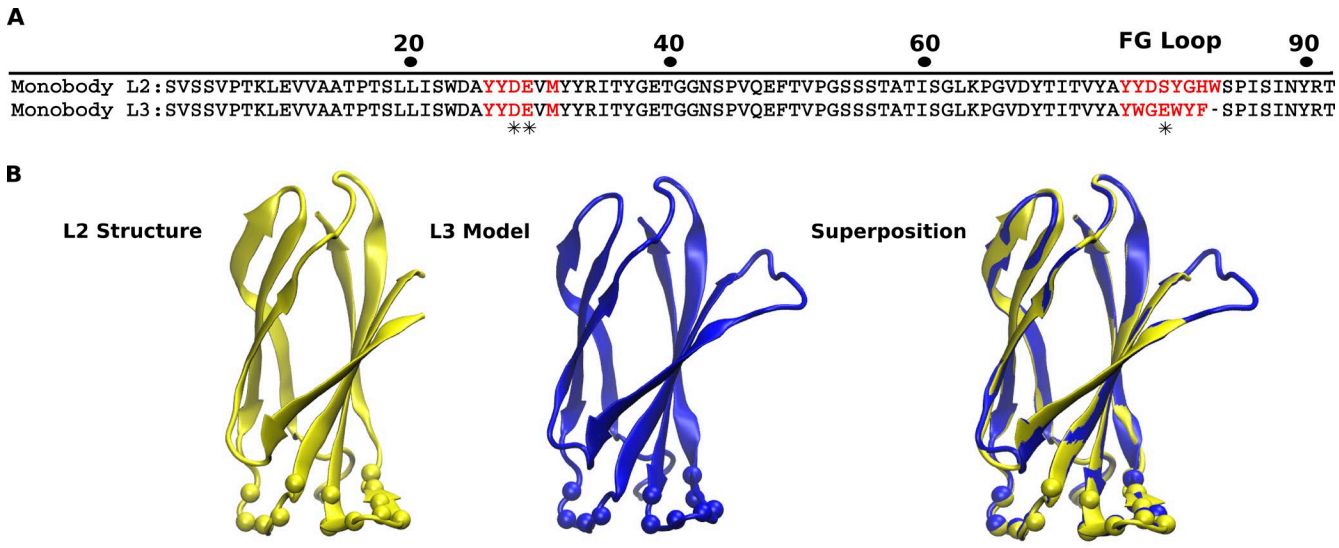

Figure 1. **Sequence and structural comparison of monobodies L2 and L3.** (A) Sequence alignment of L2 and L3. Sequences that varied during monobody selection are shown in red. Negatively charged residues in L3 near the channel binding interface are marked with asterisks. (B) Cartoon representation of L2 (yellow) and L3 homology model (blue) with residues that were varied during monobody selection represented as beads. Right, superposition of L2 and L3 homology model.

change occurs upon monobody binding that is transmitted allosterically through the channel and disrupts binding of the opposite monobody, or (2) electrostatic repulsion between oppositely bound monobodies—which carry net negative charges of three (L2) and four (L3)—destabilizes the doubly bound form. Here, we test these possibilities using equilibrium binding assays, single-channel and macroscopic electrophysiology experiments, and electrostatic calculations for WT L3, L3 electrostatic mutants, and the crystallographic monobody L2. These results support an electrostatic mechanism, with negative cooperativity originating from a single glutamate residue in L3 that extends into the aqueous vestibule between the subunits of the channel dimer. We also show that electrostatic interactions with permeant F^- ions influence monobody binding and that increasing F^- ion occupancy in the pore, either by increasing the concentration of F^- in the trans-chamber or by increasing voltage, destabilizes L3 binding. These effects are also consequences of the vestibule glutamate.

MATERIALS AND METHODS

Biochemical

Phospholipids (1-palmitoyl-2-oleoyl-*sn*-glycero-3-phosphoethanolamine [POPE], 1-palmitoyl-2-oleoyl-*sn*-glycero-3-phospho-(1'-*rac*-glycerol [POPG], and *Escherichia coli* polar lipid extract) used in reconstitution and lipid bilayer recordings were from Avanti Polar Lipids, Inc. EDANS (5-((2-aminoethyl)amino)naphthalene-1-sulfonic acid) C2 maleimide was from AnaSpec. Detergents used in purification (*n*-decylmaltoside and *n*-dodecylmaltoside) were from Anatrace.

Protein purification

The primary amino acid sequences, expression, growth, purification, and reconstitution of the Fluc homologue Bpe and monobodies, including fluorophore labeling, have been previously described (Stockbridge et al., 2014; Turman et al., 2015).

Fluorescence anisotropy

Fluorescence anisotropy experiments have been described previously (Turman et al., 2015). In brief, L3 monobodies were labeled at a unique, nonperturbing cysteine A12C with the fluorophore EDANS maleimide. For binding experiments, labeled L3 was held at a fixed concentration of 200 nM in 25 mM HEPES-NaOH, pH 7, 150 mM NaCl, 10 mM NaF, and 5 mM *n*-decylmaltoside, and Bpe concentration was varied. Each reaction was allowed to equilibrate in darkness at 21°C for 20 min before analysis using a fluorimeter (Flouromax 4; Horiba) equipped with calibrated emission and excitation polarizers. Binding isotherms were fit to a one-site binding equilibrium with total ligand as the experimental variable:

$$A([Bpe]) = A_0 + \frac{(A_f - A_0)}{2} \left(1 + \frac{[Bpe]}{[Mb]} + \frac{K_d}{[Mb]}\right)\left[1 - \sqrt{1 - \frac{4\frac{[Bpe]}{[Mb]}}{\left(1 + \frac{[Bpe]}{[Mb]} + \frac{K_d}{[Mb]}\right)^2}}\right], \quad (1)$$

where A ([Bpe]) is the anisotropy value as a function of the total Bpe, [Mb] is the fixed concentration of monobody, and A_f and A_0 are the final and initial anisotropy values.

Single-channel and macroscopic bilayer recording

Bpe proteoliposomes were prepared at 0.05 µg of protein/mg *E. coli* polar lipid extract for single-channel recordings and 10 µg/mg for macroscopic recordings and fused with a synthetic planar lipid bilayer (70% POPE/30% POPG). In all recordings, electrical ground is defined as the trans-chamber. Temperature was maintained between 21 and 23°C. Single and macroscopic block recording data were acquired as described previously (Stockbridge et al., 2014). For single-side block, voltage dependence, double-side block, and macroscopic recordings, the cis- and trans-chambers contained 15 mM MOPS, pH 7, 300 mM NaF, and, to prevent nonspecific monobody adhesion to the recording chamber, 50 µg/ml bovine serum albumin. In some experiments, the trans-F^- concentration was varied as described in the Results section (Fig. 9). Single-channel recordings acquired at voltages higher than ±100 were electronically filtered at 500 Hz to 1 kHz during acquisition and digitally filtered to 100 Hz for analysis. Recordings acquired at lower holding voltages required additional digital filtering to as low as 10 Hz for analysis. Control experiments were performed to ensure that block events were not missed as a result of filtering as described previously (Turman et al., 2015). Dwell time kinetics was calculated from single or double exponential fits to cumulative distribution histograms as described in the Results section (Fig. 5). For L3 WT and L3 E29Q, histograms contained 25–480 events per single-channel run, and for L3 E79Q, histograms contained 800–1,500 events. All data points represent the mean and SEM of at least three independent single-channel recordings. Macroscopic recordings of hundreds or thousands of channels were acquired at 1-kHz electronic filtering. Liposome fusion was allowed to proceed until a steady current level (~200 pA to 1 nA) was reached, and solution was exchanged to prevent additional fusion events. After monobody addition, current was allowed to reach steady-state levels (~10 min), and current was recorded as a mean value over a 1-min recording time.

L3 homology model and electrostatic calculations

The L3 homology model (L3–Bpe) was calculated using Modeller 9.15 software with L2–Bpe (PDB accession no. 5FXB) as the template (Webb and Sali, 2016). The automodel function was used with no additional spatial restraints. The structure with the lowest discrete protein optimized energy score was selected for further study. L3–Bpe was then explicitly centered within an 80 × 80–Å POPE membrane slab and explicitly solvated with VMD 1.9.3 solvate (Humphrey et al., 1996). Electroneutral conditions were established by placing NaCl above and below the membrane slab at 0.150 M. The simulation system comprising a channel dimer, two monobodies, POPE membrane, water, and ions consisted of 50,260 atoms with simulation dimensions of 100, 100, and 140 Å. This system was minimized and equilibrated stepwise over a total of 10 ns at 100, 200, and 300 K using NAMD 2.11, initially restraining all atoms except lipid tails, and then harmonic restraints were imposed on the protein only (Phillips et al., 2005). The final step was completed with no restraints over 2 ns. Alignment of L3–Bpe before and after minimization resulted in a root mean square (RMS) of 1.07 Å. Protein charge and radius parameters for L3–Bpe were produced with the adaptive Poisson-Boltzmann solver (APBS) using CHA RMM force field parameters. APBS and APBSmem were used to implicitly model L3–Bpe in a membrane environment (Baker et al., 2001; Callenberg et al., 2010). APBS was then used to solve the nonlinear Poisson Boltzmann equation with dielectric charge and ionic accessibility maps from APBSmem. Grid discretization was optimized to convergence for this system with grid dimensions of 161 × 161 × 161 Å and a grid length of 120 × 120 × 120 Å for grid spacing of 0.75 Å. Boundary conditions were determined by focusing from a coarse grid spacing of 1.23 Å. Per-atom electrostatic energies at E79 oxygen atoms OE1 and OE2 were used to calculate ΔE_{SF} values.

RESULTS

To visualize residues located at the L3–Bpe interface, we constructed a homology model of L3–Bpe using the L2–Bpe structure. Monobodies L2 and L3 share 93% sequence identity, differing only in the seven to eight amino acid FG loop (YYDSYGHW in L2 and YWGEWYF- in L3; Fig. 1 A; Stockbridge et al., 2014), and accordingly, the L3–Bpe homology model and L2–Bpe structure show little variation (RMS 0.36 Å; Fig. 1 B). The FG loop extends ~9 Å into the aqueous vestibules between the Bpe subunits, and three negatively charged residues are located near the L3–Bpe interface: D28 and E29, which are both conserved in L2, and E79, which is not (Fig. 2, A and B).

D28 is the most peripheral of these three residues, and in both the L3 model and the L2 structure, D28 appears to form a salt bridge with channel R66. Neutralization of this side chain, D28N, has severe consequences for L3 binding to Bpe. Although this monobody expresses and is stably folded, binding is not detectable in our biochemical assays (K_d > 15 µM; not depicted). Because neutralization of D28 is so detrimental to binding, coupled with its peripheral position, we focused on L3 residues E29 and E79. E29 does not appear to interact with any channel residue in either the L2 structure or the L3 model but is sufficiently close to the binding interface that it could plausibly contribute to the electrostatic environment. In our model, E79 is situated at the deepest point of the FG loop in the Bpe vestibule, within hydrogen bonding distance of Bpe N27 (Fig. 2 B). After

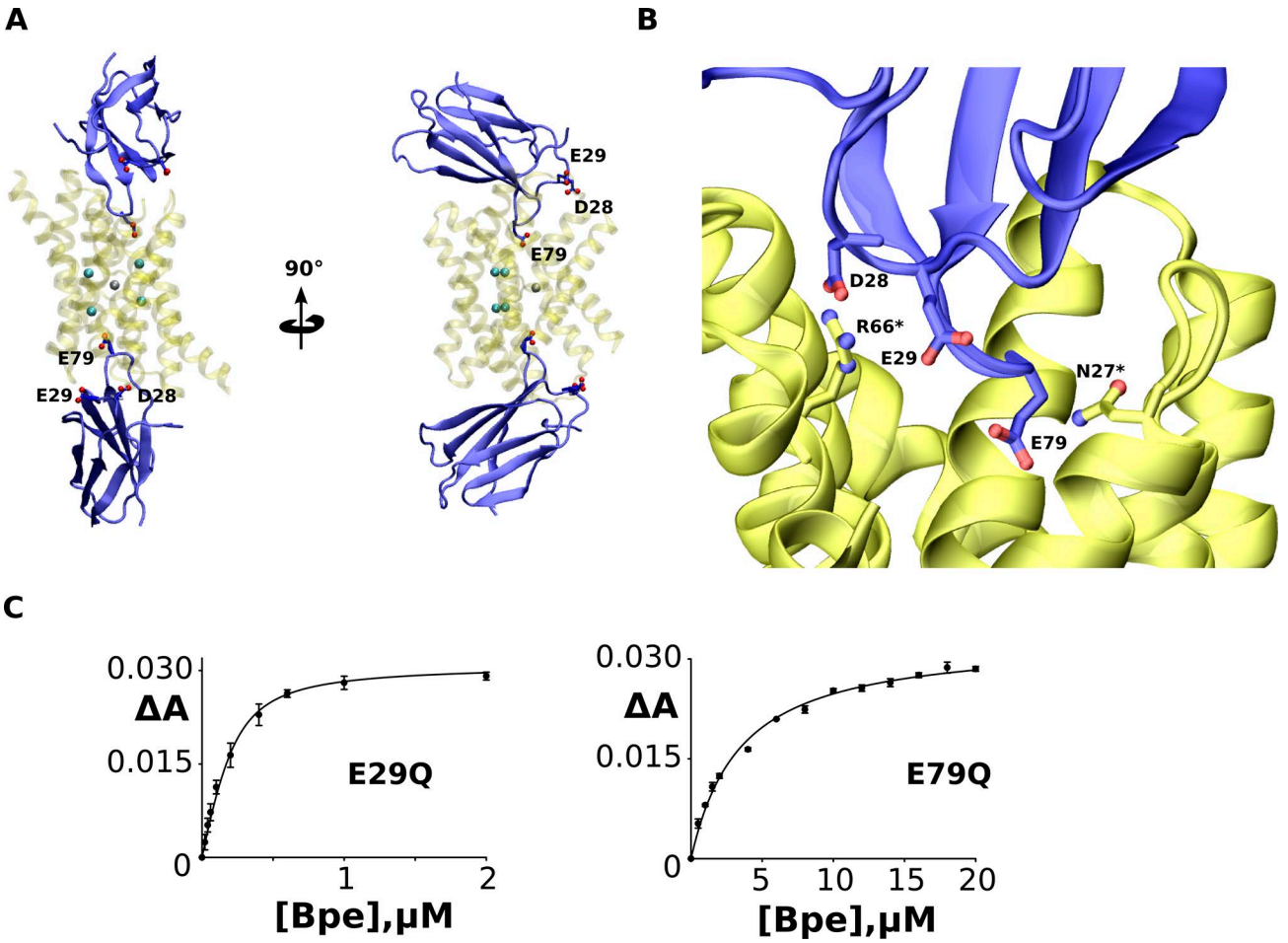

Figure 2. **Proposed L3–Bpe interface.** (A) Homology model of the Bpe channel–L3 complex with D28, E29, and E79 shown as sticks. Crystallographic F^- (cyan) and Na^+ (gray) ions are shown as spheres. (B) Detailed view of the proposed L3–channel interface, colored as in A. Proposed Bpe side chain interactions are indicated with asterisks. (C) Fluorescence anisotropy assay for association of Bpe and L3 E29Q (left) or L3 E79Q (right). The solid line represents a single-site binding isotherm that yields a K_d of 150 ± 20 nM for L3 E29Q and 3.3 ± 0.3 µM for L3 E79Q. All data points represent the mean and SEM of at least three independent measurements.

mutation of E79 and E29 individually to glutamine, the binding affinities of the mutant monobodies to detergent-solubilized Bpe were measured using fluorescence anisotropy as a function of increasing channel concentration (Fig. 2 C). These experiments do not provide an indication of binding stoichiometry but allow us to estimate the equilibrium binding affinities of ∼150 nM for E29Q and 3.3 µM for E79Q compared with 96 nM for L3 WT (Turman et al., 2015). Because of the relatively weak interaction between E79Q and channel, stoichiometry experiments using anisotropy measurements are not experimentally feasible, and we instead focused on an electrophysiological test of binding cooperativity (Turman et al., 2015).

Single-channel electrophysiological recordings with monobody applied to one side of the bilayer yielded a K_d value for L3 E29Q that is similar to L3 WT, in agreement with fluorescence anisotropy assays. WT and E29Q binding kinetics are also analogous (Fig. 3 A and Table 1). In contrast, L3 E79Q showed a marked decrease in affinity at a −200-mV holding voltage compared with L3 WT, with a K_d of 17.4 ± 0.8 µM. This effect arose from an increase in the rate of monobody dissociation and is readily apparent from the shortened nonconducting intervals (τ_{block} = 130 ± 14 ms; Fig. 3 B). Both E29Q and E79Q fluctuate between open (O) and blocked (B) states according to a simple bimolecular scheme,

$$O \underset{\beta}{\overset{\alpha}{\rightleftarrows}} B \qquad \text{(Scheme 1)}$$

$$\alpha\,[Mb] = 1/\tau_o \qquad (2a)$$

$$\beta = 1/\tau_b \qquad (2b)$$

with open intervals shortening and blocked intervals invariant as the monobody concentration is increased (Eqs. 2a and 2b; and Fig. 3, C and D).

The voltage dependence observed for L3 WT (Turman et al., 2015) also persists in L3 E29Q (Fig. 4, A and

Table 1. **Single-side monobody block**

Monobody	τ_{block}	τ_{open}	[MB]	k_{off}	k_{on}	K_d
	s	*s*		s^{-1}	$s^{-1}M^{-1}$	
L3 WT	41 ± 3	77 ± 9	30 nM	0.025	4.3×10^5	58 ± 8 nM
L3 E29Q	40 ± 7	19 ± 8	100 nM	0.025	5.4×10^5	25 ± 9 nM
L3E79Q	0.13 ± 0.01	0.19 ± 0.03	12 µM	7.7	4.4×10^5	17.4 ± 0.8 µM

B). For both L3 WT and E29Q, the mean block times decrease between −200 and 200 mV, from 45 to 2.4 s for WT and from 28 to 1.5 s for E29Q. The bulk of this increase in the rate of monobody dissociation occurs at positive voltages. Again, the behavior of L3 E79Q differs from WT and E29Q. The dissociation rate, β, is insensitive to voltage at positive voltages (Fig. 4 C) and increases by a smaller margin, approximately twofold, at negative voltages between −200 and −110 mV. These results inform the experimental design of double-sided block experiments: to ensure that block kinetics on both sides (cis and trans) are identical, both L3 E29Q and L3 E79Q must be recorded at low voltages, −25 and −100 mV, respectively. Under these conditions, the measured values of τ_{block} for both L3 E29Q and E79Q are identical within error: 22 ± 5 s (cis) and 24 ± 8 s (trans) for E29Q and 0.16 ± 0.03 s (cis) and 0.19 ± 0.05 s (trans) for E79Q.

To evaluate the contribution of the E29 and E79 side chains to the negative cooperativity observed for two-sided monobody binding, we revisited the two-sided block experiments performed previously with WT L3 (Turman et al., 2015). In these experiments, symmetrical monobody addition follows a two-state block scheme:

$$O \underset{\beta_1}{\overset{2\alpha_1}{\rightleftarrows}} B_1 \underset{2\beta_1/\Phi}{\overset{\alpha_1}{\rightleftarrows}} B_2 \qquad \text{(Scheme 2)}$$

The first monobody can bind at either of two open-channel (O) epitopes with rate $2\alpha_1$ and dissociates at rate β_1. State B_1 is a composite of singly blocked states, with monobody bound to either the cis or trans side. The presence of the double-bound state, B_2, is revealed by the emergence of longer blocked intervals that increase with increasing L3 concentration, a feature incompatible with a bimolecular reaction. Cooperativity between binding events is reflected in the dissociation

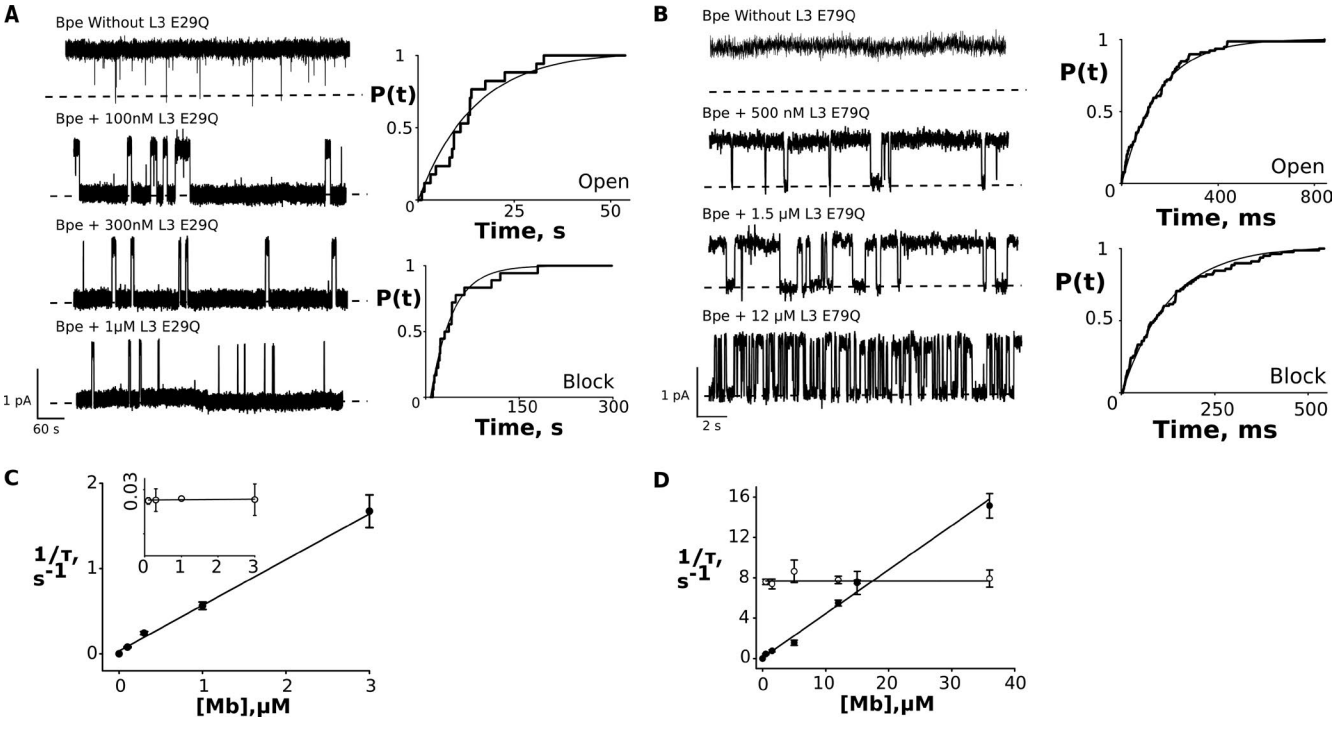

Figure 3. **Single-side block by monobody.** (A and B) Single-channel recordings of Bpe with L3 E29Q (A) and L3 E79Q (B) at indicated concentrations. Dashed lines signify zero current with channel openings shown upward. Right panels show representative cumulative distributions of block and open time intervals, with single exponential fits shown as solid smooth curves. (C and D) Bimolecular kinetics of single-side block by L3 E29Q (C) and L3 E79Q (D). Rate constants for conducting (closed circles) and nonconducting intervals (open circles) are plotted against monobody concentration. Data points represent the mean and SEM of three to five single channels, and solid lines are linear fits to data, with parameters reported in Table 1.

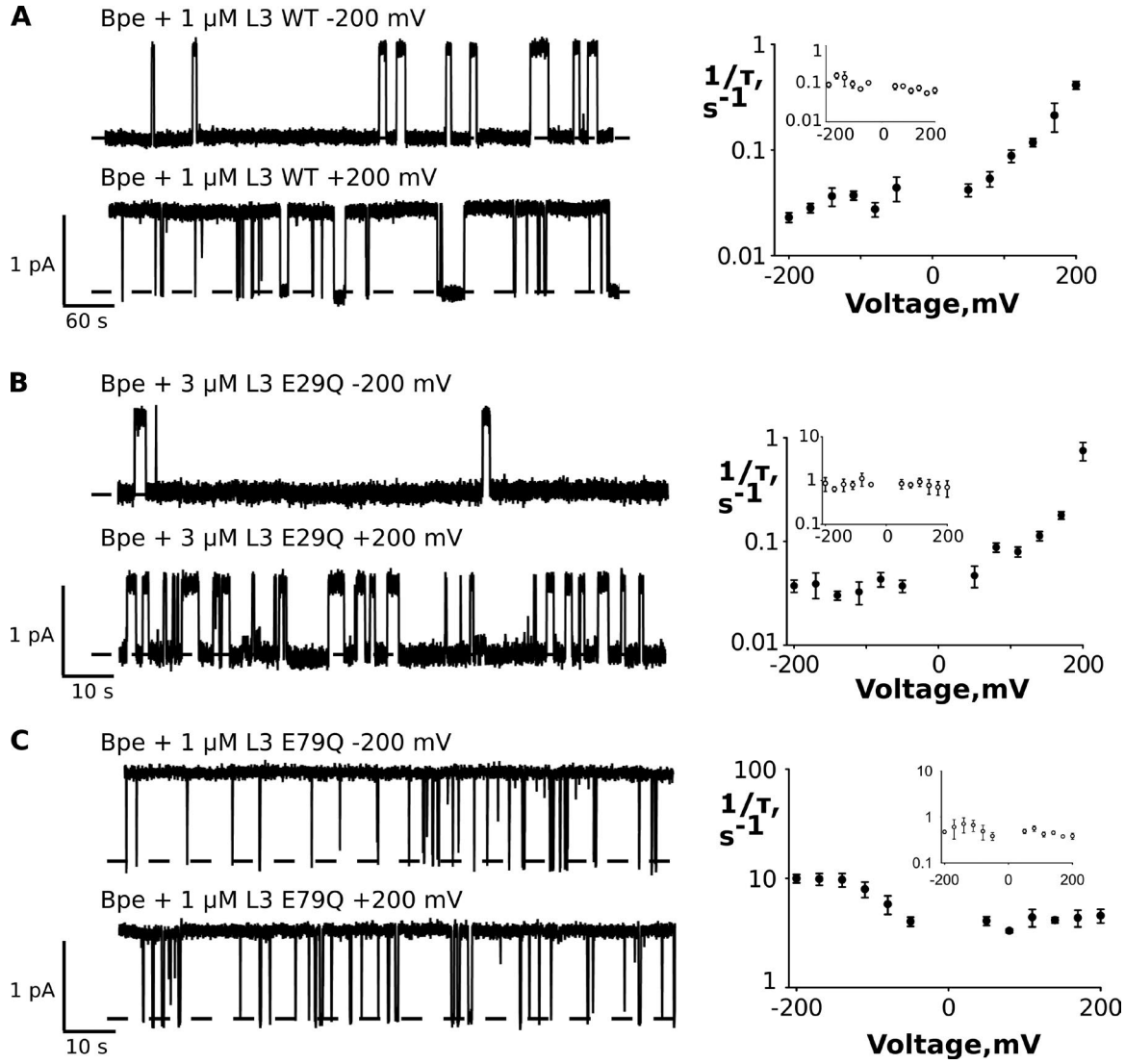

Figure 4. **Voltage dependence of single-side monobody block.** (A–C) L3 WT is shown in A, L3 E29Q is shown in B, and L3 E79Q is shown in C. Left panels show single-channel recordings of Bpe at indicated holding voltages. The dashed lines indicate the zero-current level, and channel openings are shown upward at both 200 and −200 mV. Right panels show effective rate constants for nonconducting (closed circles) and conducting intervals (inset, open circles) as a function of holding voltage. Data points and error bars represent the mean and SEM for three independent single channels.

of monobody from state B_2, $2\beta_1/\Phi$. For independent binding, Φ is unity. Negative cooperativity between two bound monobodies is reflected in a faster dissociation rate, with $\Phi < 1$. The cumulative block time distribution P(t) is given by Eqs. 3a and 3b, where M is monobody concentration and K_1 is the independently determined single-side K_d. Eqs. 3c and 3d give the amplitudes of the fast and slow fractions (Piasta et al., 2011).

$$P(t) = A_f \exp(-t/t_f) + A_s \exp(-t/t_s) \quad (3a)$$

$$\tau_{s,f} = \frac{\Phi\left(1+\frac{M}{K_1}\right)+2}{4\beta_1}\left(1 \pm \sqrt{1-\frac{8\Phi}{\left[\Phi\left(1+\frac{M}{K_1}\right)+2\right]^2}}\right) \quad (3b)$$

$$A_f = \Phi\left(1+\frac{M}{K_1}-\frac{1}{\beta_1\tau_s}\right)\cdot\frac{\tau_f}{(\tau_s-\tau_f)} \quad (3c)$$

$$A_s = 1 - A_f \quad (3d)$$

These equations make several predictions of the dwell time distributions for fast and slow block. (a) For independent binding ($\Phi = 1$), with monobody present on both sides of the channels at a concentration equal to the single-side K_d ($M/K_1 = 1$),

$$\tau_s = \frac{1}{\beta}\left(1+\sqrt{0.5}\right), \quad (3e)$$

so that the slow block intervals are 1.7× longer than $1/\beta$, the nonconducting dwell time when monobody is ap-

Table 2. **Double-side monobody block**

Monobody	Fold K_d	τ_s	τ_f[a]	A_s[a]	A_f[a]
		s	*s*		
L3 E29Q	1	28 ± 2	–	–	–
	3	32 ± 5	–	–	–
	5	31 ± 3	–	–	–
L3 E79Q	1	0.23 ± 0.04	0.021 ± 0.004	0.852 ± 006	0.148 ± 009
	3	0.37 ± 0.08	–	–	–
	5	0.62 ± 0.06	–	–	–

[a]For monobodies other than E79Q, and for [M] > 1 × K_d, the number of fast fraction events was not large enough to reliably fit to a double exponential, and the fit was therefore approximated by a single exponential. Dashes indicate that values were not extracted from the fits.

plied to a single side only. (b) When the concentration of symmetrically applied monobody is equal to the single-side K_d ($M/K_1 = 1$), the fast fraction amplitude is maximal and equal to 14.6% of the total and becomes progressively smaller as the monobody concentration increases (Fig. 5 A).

Single-channel recordings with L3 E29Q applied symmetrically to both sides resemble L3 WT recordings in their amplitude, kinetics, and affinity (Fig. 5 B and Table 2). The length of individual blocking events (~30 s) precludes observation of enough events in a single bilayer to quantify the fast fraction A_f, but because this amplitude is small relative to the slow-fraction amplitude, A_s, we can use a single exponential to fit the data and accurately extract τ_s values for the slow fraction (Fig. 5 B, bottom). Like L3 WT, L3 E29Q displays negative cooperativity of ~1.4 kcal/mol (Fig. 5 D).

In the case of L3 E79Q, with mean block times of 130 ms, thousands of blocking events can be observed from a single bilayer, revealing the biexponential cumulative

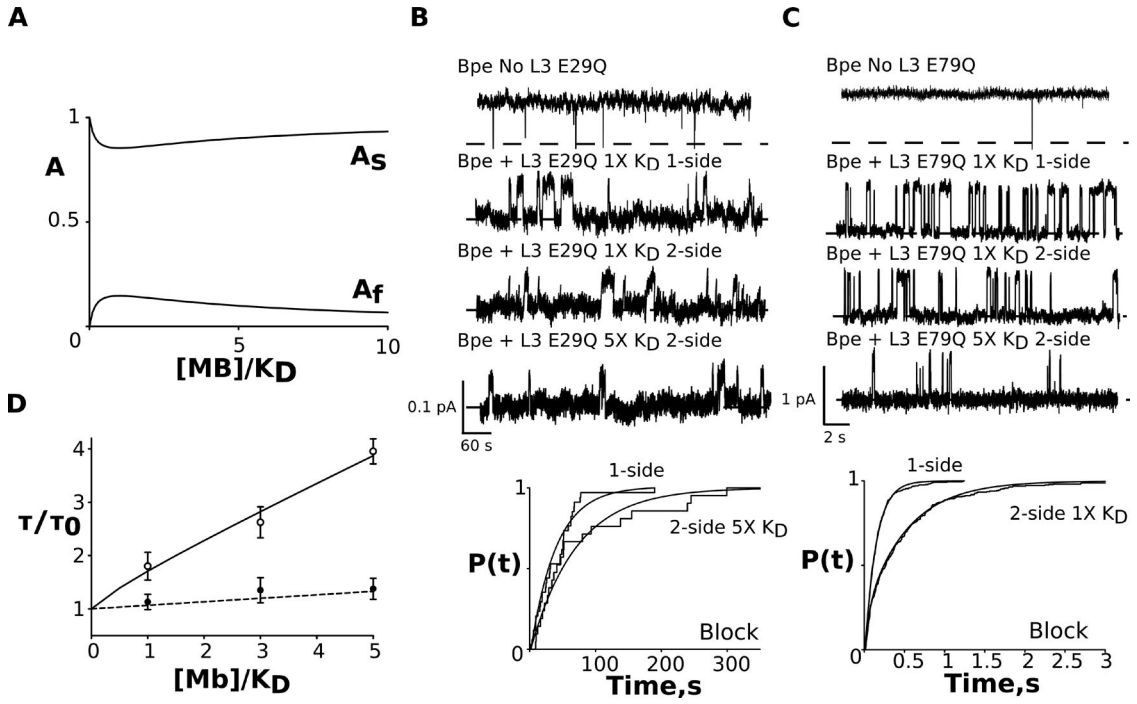

Figure 5. **Double-sided block by monobody L3 mutants.** (A) Predictions of A_f and A_s values as a function of double-sided monobody concentration according to Eqs. 3a–d. (B and C) Single-channel data for double-sided monobody block. E29Q is shown in B, and E79Q is shown in C. Top panels show single-channel bilayer recordings with monobody concentration indicated as fold K_d of independently determined single-sided monobody block. E29Q and E79Q recordings were obtained at −25 and −100 mV holding voltage, respectively. Note that the increased noise in E29Q in particular is a result of the low holding voltage. Bottom panels show representative cumulative distributions for single-sided and double-sided block experiments at indicated monobody concentrations. Single exponential (E29Q and E79Q single-sided addition) or double exponential (E79Q double-sided addition) fits are shown as smooth solid curves. (D) Double-sided block time as a function of symmetrical L3 E29Q (closed circles) and L3 E79Q (open circles) concentration. Curves represent predicted slow fraction block times for independent block (solid line) and for negatively cooperative block with $\Phi = 0.11$ (dashed line). This Φ value corresponds to the experimentally observed cooperativity factor for double-sided WT L3 binding. Data points and error bars in D are the mean and SEM determined from four to six single-channel measurements. Slow fraction block times are reported in Table 2.

block time distribution predicted by Eq. 3a. With 17 µM symmetric monobody (equal to the single-side K_d), we observe a fast fraction amplitude of 14.8% and slow fraction amplitude of 85.2%, in precise agreement with the relative amplitudes predicted by Eq. 3a. At 5× K_d, the longer blocking events are predicted to dominate, and the cumulative distribution is well approximated by a single exponential (Fig. 5 C, bottom).

Analysis of these recordings reveals that two-sided binding of L3 E79Q is not negatively cooperative (Fig. 5 D). The time constants of the long block intervals exceed the single-side block times by a factor of 1.8, which is essentially in quantitative agreement with the prediction of Eq. 3a for independent block (Table 2). At monobody concentrations equal to 3× and 5× the single-side K_d, the block times increase along the predicted isotherm for an independent double-side blocked system. Thus, neutralization of a single negative charge on the monobody, E79, is sufficient to abolish both the voltage dependence and the negative cooperativity observed for double-sided L3 block.

The rapid kinetics of E79Q, coupled with the clear resolution of the fast and slow fractions when [Mb] = K_d, also permits a kinetic comparison of the first and second monobody-binding events. Although the previous experiments demonstrated that the equilibrium constants are identical for the first and second binding event ($\Phi = 1$), they do not exclude the possibility that the kinetics are substantially different for consecutive binding events, covarying according to kinetic offset δ such that the binding constant is unchanged:

$$K_d = \frac{\delta\beta}{\delta\alpha}. \tag{4a}$$

The double-sided blocking experiment would then be described by Scheme 3:

$$O \underset{\beta}{\overset{2\alpha M}{\rightleftarrows}} \beta_1 \underset{2\beta\delta}{\overset{\alpha M\delta}{\rightleftarrows}} \beta_2 \qquad \text{(Scheme 3)}$$

For experiments performed at low monobody concentration, with [M] = K_d, Eqs. 3b–d can be rearranged according to this scheme, so that

$$\tau_{s,f} = \frac{1}{\beta} * \frac{1+3\delta}{4\delta}\left(1 \pm \sqrt{1 - \frac{8\delta}{(3\delta+1)^2}}\right) \tag{5a}$$

and

$$A_f = \left(\left(\beta + \delta\beta\right) - \frac{1}{\tau_s}\right) \cdot \frac{\tau_f}{(2\beta\delta)\left(\tau_s - \tau_f\right)}. \tag{5b}$$

The amplitudes of the fast and slow fractions are especially sensitive to δ so that if the rate constants changed by as much as a factor of 2, the amplitude of the slow fraction A_s would increase from 85.4% to 93.5 ± 2% (twofold faster kinetics) or decrease to 66.7 ± 7% (twofold slower kinetics; Fig. 6). For E79Q double-sided block with [M] = K_d (Table 2 and Fig. 5), the experimental A_s value of 85.4% corresponds to δ = 1 ± 0.2, indicating that the kinetics of the first and second monobody binding events are essentially identical and do not differ by >20%.

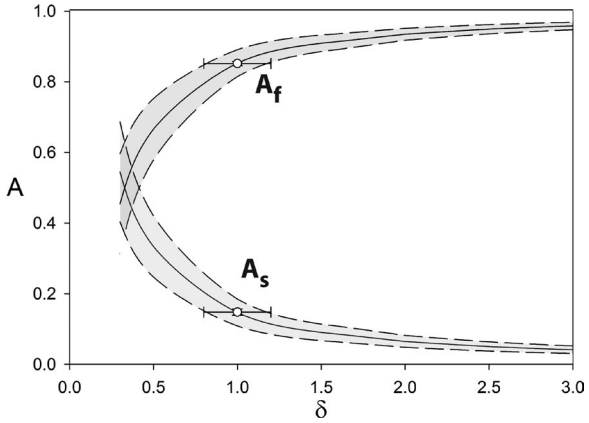

Figure 6. **Relative amplitudes of fast and slow blocks as a function of kinetic offset δ.** A_f and A_s are predicted for [M] = K_d according to Eqs. 5b and 3d, with δ values varying between 0.1 and 3 (solid lines). Dashed lines indicate standard errors in the predicted amplitudes, propagated from the standard error in the measurement of the single-sided τ_{block}. Data points are the experimental values for A_f and A_s reported in Table 2. Vertical error bars represent the SEM and are smaller than the width of the data points. Horizontal bars indicate the range of δ values consistent with the measured amplitudes, within error.

The electrophysiological experiments described so far imply that the negative cooperativity observed for double-sided L3 binding is electrostatic in origin, emanating from a single glutamate residue. In the absence of this glutamate, the second monobody binding event is identical to the first. These results predict that the blocking behavior of the crystallization monobody, L2, which lacks E79 but possesses all other negatively charged residues, should differ from that of L3: binding of L2 should not be voltage dependent and should not be negatively cooperative. L2 binding has unfavorable characteristics for evaluating single-channel block, including slow kinetics (Stockbridge et al., 2015). Therefore, we monitored macroscopic current recordings for L2, with hundreds or thousands of channels fused into the bilayer, which allows a more experimentally accessible test of voltage dependence and negative cooperativity, albeit without the kinetic detail of single-channel recordings.

To measure the voltage dependence of L2 block, the open probability (P_o) in the presence of 100 nM L2 was monitored as a function of the applied voltage from −200 to 200 mV. This was accomplished by determining the equilibrium current in the absence of L2 (I_{max}) at holding voltages between −200 and 200 mV followed by addition of L2 to the same bilayer and repetition of the current/voltage measurements. Sufficient time (>8 min) was allowed between voltage steps for the binding

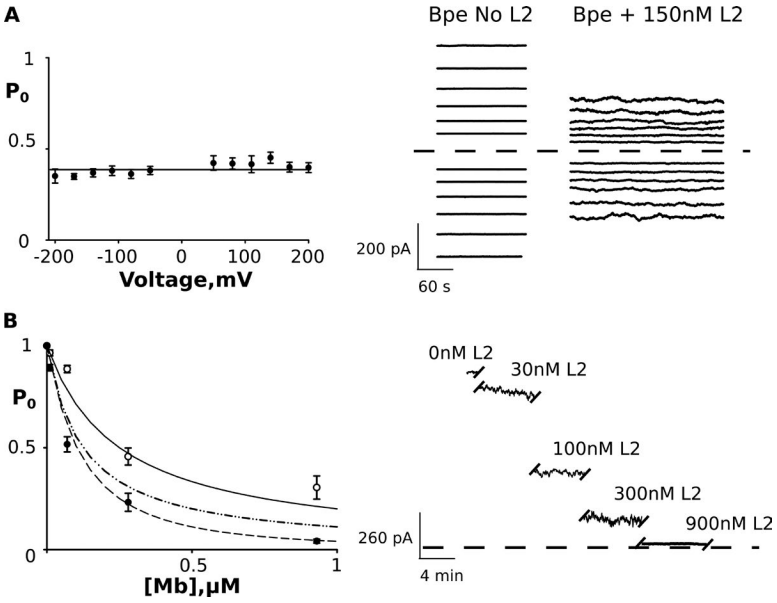

Figure 7. **Voltage dependence and double-sided block by monobody L2 in macroscopic bilayer experiments.** (A, left) Open probability (P_o) as a function of applied voltage in the presence of 150 nM L2. (Right) Representative macroscopic currents as a function of voltage in the presence and absence of L2. (B, left) Open probability as a function of L2 concentration for single-sided addition (open circles) and symmetric double-sided addition (closed circles). Predicted inhibition curves are shown for double-sided independent block (dashed line), single-sided block (solid line), and negatively cooperative block of a magnitude observed for WT L3 (Φ = 0.11; middle line). All data points represent the mean and SEM of three independent measurements. (Right) Representative macroscopic current recordings for a double-sided L2 titration experiment. The breaks indicated in these records are for the consecutive cis and trans perfusion steps, which are very noisy and typically take several minutes.

reaction to reach equilibrium. Because the individual Bpe channels are constitutively open in the absence of monobody ($P_o = 1$),

$$P_o(L2) = I_{L2}/I_{\max}. \quad (6)$$

As predicted, L2 block is voltage independent (Fig. 7 A). Next, we test whether L2 binding to the two sides of the channel occurs independently. For a single-sided monobody addition experiment, where blocking conforms with bimolecular behavior, P_o is expected to vary with monobody according to Eq. 7a:

$$P_o(Mb) = \frac{1}{1 + [Mb]/K}. \quad (7a)$$

When monobody is added to both sides symmetrically, the open probability is expected to vary with L2 concentration according to Eq. 7b:

$$P_o(Mb) = \frac{1}{1 + 2[Mb]/K + \Phi([Mb]/K)^2}, \quad (7b)$$

where $K = \beta/\alpha$ and Φ is the cooperativity factor.

For these experiments, Bpe channels were fused to the bilayer to generate macroscopic currents. After current stabilization, unfused vesicles were perfused away, and L2 was added to either the cis side only or symmetrically to both sides of the chamber. The binding reaction was allowed to reach equilibrium, and P_o was determined by comparison to the original macroscopic current as before. For single-side block experiments performed at four different L2 concentrations, P_o agrees well with the predicted bimolecular curve (Fig. 7 B). Although the relatively low dynamic range of this experiment precludes a precise measurement of the cooperativity factor, for double-sided L2 addition, the experimentally observed P_o values closely match predicted values for independent block and deviate noticeably from the curve defined by negatively cooperative binding of a magnitude observed for L3, where Φ = 0.1 (Fig. 7 B).

As one additional, independent test of the plausibility that negative cooperativity resides solely in the electrostatic interactions between the two E79 side chains, separated by 25 Å across the interior of the channel, we determined the static potential field of Bpe and the L3–Bpe complex by solving the nonlinear Poisson-Boltzmann equation and compared the energies (ΔE_{SF}) of the E79 side chain carboxylate in those fields. We find that ΔE_{SF} at E79 increases when a second, oppositely bound WT L3 is present (Fig. 8 A) and that this value increases as the computationally varied dielectric constant decreases. Destabilization by the second L3 molecule can be observed at dielectric values below ~10. When $\Delta\Delta E_{SF}$ is equal to the experimentally determined negative cooperativity (1.4 kcal/mol), the protein dielectric value is 4.8 (Fig. 8 B). That this latter value is reasonable (Gilson and Honig, 1986; Li et al., 2013) reaffirms that electrostatic repulsion between the two vestibule glutamates could, by itself, account for the negative cooperativity. Consistent with electrophysiological data, ΔE_{SF} of E29 is comparatively insensitive to the presence of a monobody bound in trans, and when the oppositely bound monobody bears an E79Q mutation, its presence is not destabilizing (Fig. 8, B and C).

Finally, we address a natural corollary to our investigation of the electrostatic relationships that influence monobody binding: whether F^- ions bound within the pores similarly exert an electrostatic influence on L3 monobody binding. To evaluate this experimentally, we monitored the blocking behavior of monobody L3 applied to the cis side of the bilayer as a function of increasing trans-F^- from 0 to 600 mM (Fig. 9). To maintain

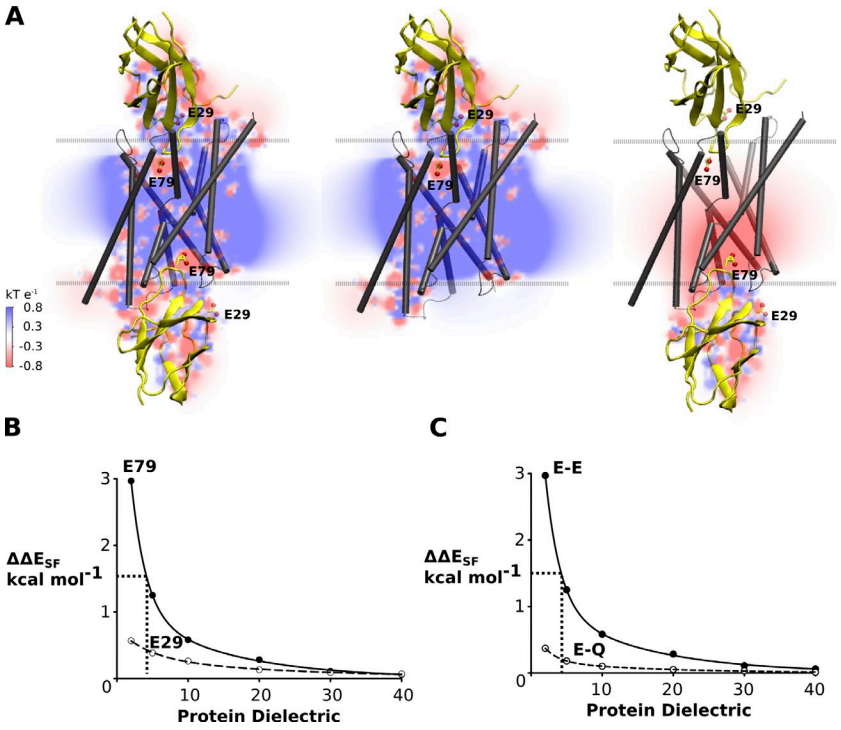

Figure 8. **APBS calculations of electrostatic destabilization by oppositely bound L3 monobody.** (A) Electrostatic potential maps calculated at a protein dielectric of five for doubly bound Bpe (left) and singly bound Bpe (middle), with the difference map shown at right. (B) Difference in static field energy at E79 (closed circles) and E29 (open circles) in the presence and absence of a second monobody bound in trans as a function of dielectric. (C) Difference in the static field energy at E79 with WT (closed circles) or E79Q (open circles) monobody bound in trans as a function of dielectric. All data points represent the mean of at least three independent single-channel recordings.

ionic strength in the trans-chamber, F^- was supplemented with inert counter ions, Cl^- or isethionate. On a background of 600 mM F^-, neither influenced the kinetics of monobody binding in the cis-chamber at concentrations up to 600 mM.

With L3 WT and L3 E29Q, increasing trans-F^- leads to reductions in block time intervals, whereas the open intervals remain the same (Fig. 9, A and B; and Table 3). WT L3 is approximately twofold more sensitive to the trans-F^- effect than E29Q. L3 E79Q, in contrast, is insensitive to varied trans-F^- (Fig. 9 C). Thus, the trans enhanced dissociation effect is limited to monobodies (L3 and L3 E29Q) that bind with a glutamate residue (E79) extending into the vestibule, suggesting that as F^- ion is increased in the trans-chamber and ion-binding sites are populated within the pores, the ions electrostatically destabilize the bound monobody. The absence of an effect on the monobody association rate indicates that the destabilization is not competitive. The effect is modest, with a maximum destabilization of about fivefold, or 1 kcal/mol. Although the overall destabilization is somewhat less than observed for, for example, charybdotoxin and K^+ channels (MacKinnon and Miller, 1988; Park and Miller, 1992), the knockoff effect saturates at a similar ion concentration of ~600 mM (Fig. 9, A and B).

DISCUSSION

The results described here provide a comprehensive picture of electrostatic relationships between the binding of monobody inhibitors and transient ions to Fluc family F^- channels. We show that rationalizing the negative cooperativity between distal monobody-binding events need not invoke a conformational change in the channel but can be readily explained by cross-channel electrostatic destabilization alone. The more surprising result is that the negative cooperativity is not a function of the monobody's net −4 charge but instead resides solely in a single glutamate side chain that extends into the channel's aqueous vestibule, functionally reminiscent of other peptide toxins such as the pore-binding lysine of charybdotoxin (Park and Miller, 1992; Goldstein and Miller, 1993; Banerjee et al., 2013). Neutralization of this single glutamate by mutation to glutamine abolishes negative cooperativity, whereas neutralizing mutation of another charged residue near the channel interface, E29, does not have this effect. It is notable that the monobodies that were useful as crystallization chaperones lack an analogous carboxylate side chain along with the associated functional signatures like negative cooperativity and voltage dependence of block. Because all three Fluc–monobody complexes reported to date (Stockbridge et al., 2015) are in a doubly bound conformation, it seems likely that having monobodies bound at both epitopes increases the likelihood of constructive crystal packing and that for monobody variants with a vestibule carboxylate, the energetic penalty incurred for binding both simultaneously precludes crystallization.

These results also serve to further characterize the mechanism of channel block by monobody L3. L3 binding shows a pronounced voltage dependence at positive voltage but flattens at negative voltages, inconsistent

Table 3. **Trans-F^- destabilization**

Monobody	β_{Min}	β_{Max}	K_d
	s^{-1}	s^{-1}	mM
L3 WT	0.019 ± 0.004	0.16 ± 0.09	373 ± 43
L3 E29Q	0.023 ± 0.009	0.083 ± 0.008	542 ± 37
L3 E79Q	9.6 ± 0.4	9.6 ± 0.9	NA

NA, not applicable.

with the Woodhull model of voltage-dependent binding (Woodhull, 1973). Considered alongside the enhanced rate of dissociation as the trans-F^- concentration increases, it is evident that populating F^--binding sites within the channel, either by increasing concentration or by driving channel occupancy with increasing voltage, destabilizes bound L3. Mutagenic evidence supports the idea that the four F^- ions observed in the crystal structure demarcate the conducting pores (Stockbridge et al., 2015; Last et al., 2016), but, because of the unusually complicated double-barreled architecture and uncertainty about the route by which ions reach these binding sites, it is not clear which, if any, of these crystallographic ions is responsible for the electrostatic effects observed here.

Although these classical indicators strongly imply a physical mechanism of pore block by L3 (MacKinnon and Miller, 1988), they still do not rule out a monobody-induced allosteric channel closing to explain the inhibition of current. A third observation from our experiments with E79Q, however, would appear to dispel any remaining possibility of an allosteric mechanism for this monobody. These experiments not only showed

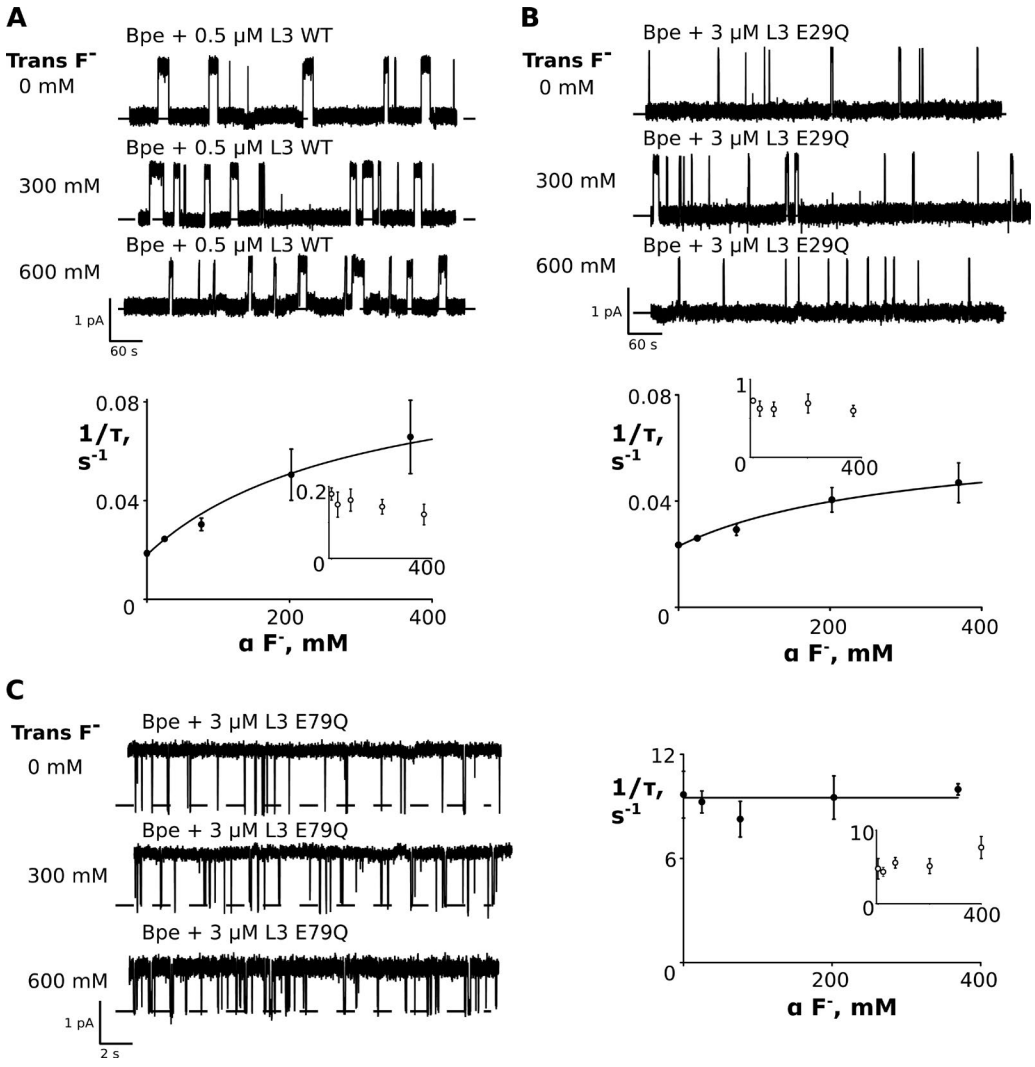

Figure 9. **Monobody binding as a function of trans-F^- activity.** (A–C) L3 WT block is shown in A, L3 E29Q is shown in B, and L3 E79Q is shown in C. Single-channel recordings show Bpe with constant cis-monobody and trans-F^- activity varied as indicated. Plots show effective rate constants for blocked (closed circles) and conducting intervals (inset, open circles) as a function of trans-F^- activity. Data points and error bars are the mean and SEM for three to four single channels. Solid lines show fits to a rectangular hyperbola binding isotherm with fit parameters reported in Table 3.

that negative cooperativity is abolished in this mutant—that is, that the equilibrium constants for the first and second monobody binding event are identical—but also that the kinetics are identical within the error of the measurement. This provides a persuasive argument that the conformation of the channel is unchanged upon the first monobody binding event, an observation that is incompatible with allosteric inhibition.

ACKNOWLEDGMENTS

We thank Christopher Miller (Brandeis University) for his support of this project and for helpful discussions and unrelenting criticism. We also thank Janice Robertson (University of Iowa) for helpful discussions and critical reading of the manuscript.

This work was supported, in part, by National Institutes of Health grant R00-GM111767 to R.B. Stockbridge. D.L. Turman is supported by the Howard Hughes Medical Institute in the laboratory of Christopher Miller.

The authors declare no competing financial interests.

Author contributions: R.B. Stockbridge and D.L. Turman designed and performed experiments, analyzed the data, and wrote the paper.

Richard W. Aldrich served as editor.

Submitted: 20 December 2016
Accepted: 3 February 2017

REFERENCES

Baker, J.L., N. Sudarsan, Z. Weinberg, A. Roth, R.B. Stockbridge, and R.R. Breaker. 2012. Widespread genetic switches and toxicity resistance proteins for fluoride. *Science.* 335:233–235. http://dx.doi.org/10.1126/science.1215063

Baker, N.A., D. Sept, S. Joseph, M.J. Holst, and J.A. McCammon. 2001. Electrostatics of nanosystems: application to microtubules and the ribosome. *Proc. Natl. Acad. Sci. USA.* 98:10037–10041. http://dx.doi.org/10.1073/pnas.181342398

Banerjee, A., A. Lee, E. Campbell, and R. Mackinnon. 2013. Structure of a pore-blocking toxin in complex with a eukaryotic voltage-dependent K^+ channel. *eLife.* 2:e00594. http://dx.doi.org/10.7554/eLife.00594

Callenberg, K.M., O.P. Choudhary, G.L. de Forest, D.W. Gohara, N.A. Baker, and M. Grabe. 2010. APBSmem: a graphical interface for electrostatic calculations at the membrane. *PLoS One.* 5:e12722. http://dx.doi.org/10.1371/journal.pone.0012722

Gilson, M.K., and B.H. Honig. 1986. The dielectric constant of a folded protein. *Biopolymers.* 25:2097–2119. http://dx.doi.org/10.1002/bip.360251106

Goldstein, S.A., and C. Miller. 1993. Mechanism of charybdotoxin block of a voltage-gated K+ channel. *Biophys. J.* 65:1613–1619. http://dx.doi.org/10.1016/S0006-3495(93)81200-1

Humphrey, W., A. Dalke, and K. Schulten. 1996. VMD: visual molecular dynamics. *J. Mol. Graph.* 14:33–38: 27–28. http://dx.doi.org/10.1016/0263-7855(96)00018-5

Ji, C., R.B. Stockbridge, and C. Miller. 2014. Bacterial fluoride resistance, Fluc channels, and the weak acid accumulation effect. *J. Gen. Physiol.* 144:257–261. http://dx.doi.org/10.1085/jgp.201411243

Koide, A., J. Wojcik, R.N. Gilbreth, R.J. Hoey, and S. Koide. 2012. Teaching an old scaffold new tricks: monobodies constructed using alternative surfaces of the FN3 scaffold. *J. Mol. Biol.* 415:393–405. http://dx.doi.org/10.1016/j.jmb.2011.12.019

Last, N.B., L. Kolmakova-Partensky, T. Shane, and C. Miller. 2016. Mechanistic signs of double-barreled structure in a fluoride ion channel. *eLife.* 5:e18767. http://dx.doi.org/10.7554/eLife.18767

Li, L., C. Li, Z. Zhang, and E. Alexov. 2013. On the dielectric "constant" of proteins: smooth dielectric function for macromolecular modeling and its implementation in DelPhi. *J. Chem. Theory Comput.* 9:2126–2136. http://dx.doi.org/10.1021/ct400065j

MacKinnon, R., and C. Miller. 1988. Mechanism of charybdotoxin block of the high-conductance, Ca2+-activated K+ channel. *J. Gen. Physiol.* 91:335–349. http://dx.doi.org/10.1085/jgp.91.3.335

Park, C.S., and C. Miller. 1992. Interaction of charybdotoxin with permeant ions inside the pore of a K^+ channel. *Neuron.* 9:307–313. http://dx.doi.org/10.1016/0896-6273(92)90169-E

Phillips, J.C., R. Braun, W. Wang, J. Gumbart, E. Tajkhorshid, E. Villa, C. Chipot, R.D. Skeel, L. Kalé, and K. Schulten. 2005. Scalable molecular dynamics with NAMD. *J. Comput. Chem.* 26:1781–1802. http://dx.doi.org/10.1002/jcc.20289

Piasta, K.N., D.L. Theobald, and C. Miller. 2011. Potassium-selective block of barium permeation through single KcsA channels. *J. Gen. Physiol.* 138:421–436. http://dx.doi.org/10.1085/jgp.201110684

Stockbridge, R.B., J.L. Robertson, L. Kolmakova-Partensky, and C. Miller. 2013. A family of fluoride-specific ion channels with dual-topology architecture. *eLife.* 2:e01084.

Stockbridge, R.B., A. Koide, C. Miller, and S. Koide. 2014. Proof of dual-topology architecture of Fluc F- channels with monobody blockers. *Nat. Commun.* 5:5120. http://dx.doi.org/10.1038/ncomms6120

Stockbridge, R.B., L. Kolmakova-Partensky, T. Shane, A. Koide, S. Koide, C. Miller, and S. Newstead. 2015. Crystal structures of a double-barrelled fluoride ion channel. *Nature.* 525:548–551. http://dx.doi.org/10.1038/nature14981

Turman, D.L., J.T. Nathanson, R.B. Stockbridge, T.O. Street, and C. Miller. 2015. Two-sided block of a dual-topology F- channel. *Proc. Natl. Acad. Sci. USA.* 112:5697–5701. http://dx.doi.org/10.1073/pnas.1505301112

Webb, B., and A. Sali. 2016. Comparative protein structure modeling using MODELLER. *Curr. Protoc. Protein Sci.* 86:2.9.1–2.9.37. http://dx.doi.org/10.1002/cpps.20

Woodhull, A.M. 1973. Ionic blockage of sodium channels in nerve. *J. Gen. Physiol.* 61:687–708. http://dx.doi.org/10.1085/jgp.61.6.687